ERJ
Engineering Research Journal
Faculty of Engineering
Minoufiya University

NUMERICAL AND EXPERIMENTAL INVESTIGATION OF COMPRESSIBLE FLOW EJECTORS

N. I. I. Hewedy, Mofreh H. Hamed, F. Sh. Abou-Taleb and Tarek A. Ghonim

Mechanical Power Engineering Department
Faculty of Engineering, Menoufiya University, Shebin El-Kom, Egypt
E-mail: mofrehhh@ yahoo.com

ABSTRACT

The present work deals with numerical and experimental investigation of supersonic air-air ejectors. The numerical investigation is based on flow equations governing turbulent, compressible, two-dimensional, steady, time averaged and boundary layer equations. These equations are continuity, momentum and energy. In addition, turbulent shear stress and heat transfer are calculated using eddy viscosity model. These equations are solved iteratively using finite difference method under the conditions of different flow regimes which can be divided into several distinctive regions where, the methods for estimating the mixing length are different for each flow region. The first region depicts the wall boundary layer, jet shear layer and secondary and primary potential flow. The second one contains a single region of developing flow. The present results are concerned with the static pressure coefficient, temperature and velocity distributions along the mixing duct and diffuser. Also the overall efficiency of the ejectors for different flow conditions such as, motive air stagnation pressure and temperature, secondary air temperature and mass ratio is calculated. A simple ejector with convergent-divergent primary nozzle was fabricated and experimentally tested. The present theoretical and experimental results are compared with published data. This comparison shows a good agreement. The results obtained help to understand the flow behavior and physical phenomena occurring in the flow through ejectors.

هذه الورقة تدرس عدديا ومعمليا سريان (هواء–هواء) فوق سرعة الصوت خلال حاقن نافورى. الدراسة العددية تعتمد على المعادلات الخاصة بالسريان الأضطرابى الأنضغاطى ثنائي الأبعاد المستقروهي معادلات الاستمرارية و بقاء كمية التحرك وبقاء الطاقة ومعادلات الطبقة المتاخمة. كما تم استخدام نموذج أدى في حساب انتقال الحرارة و الاحتكاك الأضطرابى. تم حل المعادلات السابقة بطريقه تكراريه باستخدام طريقة الفروق المحدده. نتائج هـذه الدراسة تختص بتوزيع معامل الضغط الأستاتيكى و درجة الحرارة و السرعة على طول غرفة الخلط و الناشر. أيضا تم حساب الكفاءة الكلية للحاقن عند ظروف تشغيل مختلفة من ضغط حقن و درجة حرارة للمائع الأولي و نسبة معدل التدفق لكلا المائعين. و للدراسة المعملية تم تصنيع نموذج لحاقن نافورى متغير المقطـع و اختبـاره عمليا. ولأختبار النموذج المقترح فقد تم عمل مقارنه بين نتائج البحث النظرية و المعملية الحاليـة والمعمليـة و النظرية المنشورة لآخرين و أظهرت هذه المقارنة توافقا مقبولا. تساعدنا النتائج في فهم نظرية عمل و أداء الحقن كما توضح أهمية اختيار الأبعاد المناسبة لظروف تشغيل معينه للحصول علي أداء عالي الكفاءة.

Keywords: Supersonic flow, two-dimensional flow, turbulent and heat transfer, ejectors.

1. INTRODUCTION

Supersonic ejectors are widely used in many applications such as aerospace, propulsion and refrigeration. Ejector performance has been studied experimentally and numerically by many researchers. Fabri and Paulon [1] studied experimentally and theoretically supersonic air-air ejectors. The theoretical analysis was based on one-dimensional flow and experimental study was conducted on a constant-area mixing ejector. The effects of different parameters such as length of the mixer, terminating diffuser length, cross section of the mixer and primary flow Mach number were studied theoretically. Barna [2] investigated experimentally the aerodynamic performance and noise generation characteristics of five constant-area mixing ejectors having subsonic secondary flow. The investigations given in [1, 2] were carried out on constant-area mixing ejectors. It is well known that constant-pressure mixing ejectors have a better performance than the constant-area mixing ejectors which were investigated by [1, 2]. Hickman et al. [3] developed an analytical model to predict the performance characteristics of two-dimensional axisymmetric single-nozzle ejector with variable area mixing tubes "constant-pressure mixing". Abou-taleb [4] studied experimentally and analytically the effect of

geometric parameters on the performance of ejectors. Approximate formulae for calculating pressure ratio and optimum entrainment ratio as well as the optimum design conditions were derived. Raman and Taghavi [5] provided a detailed experimental evaluation of a rectangular multi-element supersonic jet mixer-ejector nozzle. The obtained results show that the ejector configuration that produced the maximum entrainment ratio also exhibited the lowest wall pressures in the inlet region and maximum thrust augmentation. Huang et al. [6] carried out a one-dimensional analysis for the prediction of ejector performance at critical-mode operation. Experiments using 11 ejectors were conducted to verify the analytical results. The test results were used to determine the coefficients defined in the 1-D model by matching the test data with the analytical results. Several assumptions were made in their model. De Chant and Nadell [7] developed a system of analytical and numerical two-dimensional mixer/ejector nozzle models that required minimal empirical input. Four sample problems, three ejector nozzles and one mixer nozzle were studied. De Chant et al. [8] extended the work given in [7] by developing an enhanced modeling which extends beyond the simple primary/secondary mixing configuration to a multiple stream forced and entrained mixing capability. Szabo [9] studied analytically the influence of the material quality of the primary gas jets on the final vacuum created by a supersonic gas ejector. Examined ejectors showed that their geometry greatly depended on the quality changes of the operating primary gas due to temperature and pressure changes. Arbel et al. [10] analyzed and characterized the irreversibility of the ejector's internal processes in an effort to improve its overall performance. The analysis was based on entropy production methodology. Bartosiewicz et al. [11] investigated experimentally and numerically the performance of supersonic ejectors. In the numerical investigation six well-known turbulence models were used. The tested model turned out to be an efficient diagnosis tool of ejector analysis and performance optimization (optimum entrainment and recompression ratios). Kandakure et al. [12] developed a numerical model to understand the hydrodynamic characteristics with reference to ejector geometry and the effects of operating conditions on the ejector performance. Most of previous literature have not investigated the effects of inflow parameters on the ejector efficiency. Therefore in the present study the effects of inflow parameters on the ejector performance especially its efficiency and ejector mass ratio are experimentally and numerically investigated. In addition the effect of heat transfer between the motive fluid and the entrained fluid is also studied.

2. EXPERIMENTAL SETUP

The experimental installation is schematized in Fig. (1). Compressor of sufficient capacity is used to ensure the continuous operation of the ejector. Compressed air (at a maximum pressure of about 8 bar and an ambient stagnation temperature) is filtered to remove large particles such as dust and compressed oil droplets. The compressed air is then directed towards an air reservoir which is connected to the entrance of the primary flow nozzle of the ejector just after passing through a pressure control valve to adjust the primary flow stagnation pressure P_{o1}. The entrained air flow is taken from the surrounding atmosphere. The entrained mass flow rate can be regulated by means of a valve located at the entrance of the aspiration tube.

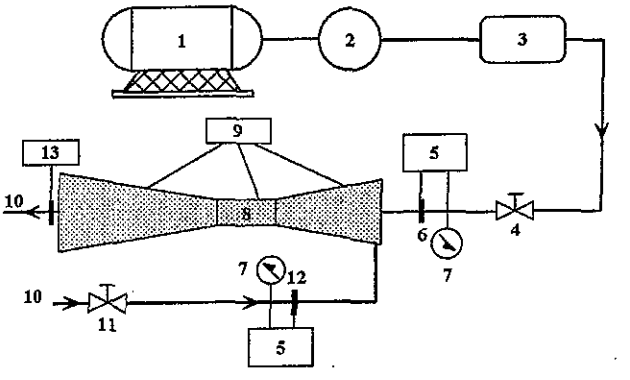

1- Air compressor
2- Air filter
3- Compressed air reservoir
4- Pressure control valve
5- U-tube manometer
6- Pitot-static tube of motive flow
7- Pressure gage
8- Tested ejector
9- Multi-U-tube manometer
10- Surrounding atmosphere
11- Throttling valve
12- Pitot-static tube of sucked flow
13- Pitot tube of total flow

Fig. (1) Experimental setup.

Apparatuses installed on the primary and secondary air circuits to measure the stagnation pressures and mass flow rates are also shown in Fig. (1). Wall static pressure measurements along the ejector were measured using an inclined multi-U-tube manometer.

In the tested ejector as illustrated in Fig. (2), the exit diameter of the primary flow nozzle is 6.2 mm (inner), the dimensionless constant pressure mixing section length (La/Db), constant area mixing section length (Lb/Db), diffuser section length (Lc/Db) and area ratio (Ar) are 4.08, 4.46, 8.9 and 17.38 respectively while the total angles of the constant pressure mixing section and the diffuser section, θ_1 and θ_2, are 5.456° and 2.664° respectively. The uncertainty for all the measuring devices is found to be in the range of 0.002% to 5.55%.

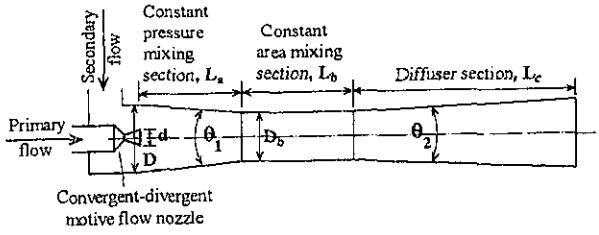

Fig. (2) Typical ejector geometry.

3. MATHEMATICAL MODEL

The flow through the ejector is modeled on the governing flow equations based on the following assumptions:

- Two dimensional and steady flow.
- Both steam flows are the same perfect gas.
- No heat transfer across the walls of the ejector.
- Both streams are assumed to be shockless.
- Static pressure is constant at any section normal to the axial direction.

3.1. Governing Equations

The conservation equations governing turbulent, compressible, two-dimensional, steady, time-averaged and boundary layer are continuity, momentum and energy equations.

- Continuity Equation

$$\frac{\partial \bar{\rho}\,\bar{u}}{\partial x} + \frac{1}{y^{\alpha}}\frac{\partial\left(\bar{\rho}\,\bar{v}\,y^{\alpha}\right)}{\partial y} = 0 \qquad (1)$$

- Momentum Equation

$$\bar{\rho}\,\bar{u}\frac{\partial \bar{u}}{\partial x} + \bar{\rho}\,\bar{v}\frac{\partial \bar{u}}{\partial y} = -\frac{d\bar{p}}{dx} + \frac{1}{y^{\alpha}}\frac{\partial}{\partial y}\left[\bar{\mu}\,y^{\alpha}\frac{\partial \bar{u}}{\partial y} - y^{\alpha}\,\overline{u'(\rho v)'}\right] \qquad (2)$$

- Energy Equation

$$\bar{\rho}\,\bar{u}\,\bar{c}_p\frac{\partial \bar{T}}{\partial x} + \bar{\rho}\,\bar{v}\,\bar{c}_p\frac{\partial \bar{T}}{\partial y} = \bar{u}\frac{\partial \bar{p}}{\partial x} + \bar{\mu}\left(\frac{\partial \bar{u}}{\partial y}\right)^2 + \frac{1}{y^{\alpha}}\frac{\partial}{\partial y}\left[\bar{k}\,y^{\alpha}\frac{\partial \bar{T}}{\partial y} - \bar{c}_p\,y^{\alpha}\overline{(\rho v)'T'}\right] - \overline{u'(\rho v)'}\frac{\partial \bar{u}}{\partial y} \qquad (3)$$

Where $\alpha = 1$, $y = r$ for axisymmetric flow and $\alpha = 0$ for two-dimensional flow.

For axisymmetric flow, the above system of equations can be rewritten in terms of stream function, ψ using the proposed transformation by Krause [13] as follows:

$$\bar{u}\frac{\partial \bar{u}}{\partial x} = -\frac{1}{\bar{\rho}}\frac{d\bar{p}}{dx} + \frac{\bar{u}}{2\psi}\frac{\partial}{\partial \psi}\left[\frac{\bar{\mu}\,\bar{\rho}\,\bar{u}\,r^2}{2\psi}\frac{\partial \bar{u}}{\partial \psi} - \overline{u'(\rho v)'}\,r\right] \qquad (4)$$

$$\bar{u}\,\bar{c}_p\frac{\partial \bar{T}}{\partial x} = \frac{\bar{u}}{\bar{\rho}}\frac{\partial \bar{p}}{\partial x} + \frac{\Phi}{\bar{\rho}} + \frac{\bar{u}}{2\psi}\frac{\partial}{\partial \psi}\left[\frac{\bar{k}\,\bar{\rho}\,\bar{u}\,r^2}{2\psi}\frac{\partial \bar{T}}{\partial \psi} - \bar{c}_p\,\overline{T'(\rho v)'}\,r\right] \qquad (5)$$

Where,

$$\Phi = \left(\frac{\bar{\rho}\,\bar{u}\,r}{2\psi}\frac{\partial \bar{u}}{\partial \psi}\right)^2 - \overline{u'(\rho v)'}\left(\frac{\bar{\rho}\,\bar{u}\,r}{2\psi}\frac{\partial \bar{u}}{\partial \psi}\right)$$

$$\frac{\partial \psi^n}{\partial y} = \bar{\rho}\,\bar{u}\,r^{\alpha} \quad ; \quad \frac{\partial \psi^n}{\partial x} = \bar{\rho}\,\bar{v}\,r^{\alpha}$$

Since, n is an integer value greater than one, in the present study $n = 2$.

Using the eddy viscosity model, the "turbulent shear stress" and "turbulent heat transfer" are defined by:

$$\tau_T = \bar{\rho}\,\varepsilon\frac{\partial \bar{u}}{\partial r} = -\overline{u'(\rho v)'} = \frac{\bar{\rho}^2\,\bar{u}\,r\,\varepsilon}{2\psi}\frac{\partial \bar{u}}{\partial \psi} \qquad (6)$$

$$q_T = \bar{\rho}\,\bar{c}_p\varepsilon_H\frac{\partial \bar{T}}{\partial r} = -\bar{c}_p\overline{(\rho v)'T'} = \frac{\bar{\rho}^2\,\bar{u}\,r}{2\psi}\bar{c}_p\varepsilon_H\frac{\partial \bar{T}}{\partial \psi} \qquad (7)$$

Where ε is termed the "eddy momentum diffusivity" and ε_H is the "eddy thermal diffusivity".

After substitution from equations (6) and (7), equations (4) and (5) become:

$$\bar{u}\frac{\partial \bar{u}}{\partial x} = -\frac{1}{\bar{\rho}}\frac{d\bar{p}}{dx} + \frac{\bar{u}}{2\psi}\frac{\partial}{\partial \psi}\left[\frac{\left(\bar{\mu}+\bar{\rho}\,\varepsilon\right)\bar{\rho}\,\bar{u}\,r^2}{2\psi}\frac{\partial \bar{u}}{\partial \psi}\right] \qquad (8)$$

$$\bar{u}\,\bar{c}_p\frac{\partial \bar{T}}{\partial x} = \frac{\bar{u}}{\bar{\rho}}\frac{\partial \bar{p}}{\partial x} + \frac{\left(\bar{\mu}+\bar{\rho}\,\varepsilon\right)}{\bar{\rho}}\left(\frac{\bar{\rho}\,\bar{u}\,r}{2\psi}\frac{\partial \bar{u}}{\partial \psi}\right)^2 + \frac{\bar{u}}{2\psi}\frac{\partial}{\partial \psi}\left[\left(\bar{k}+\bar{\rho}\,\bar{c}_p\varepsilon_H\right)\frac{\bar{\rho}\,\bar{u}\,r^2}{2\psi}\frac{\partial \bar{T}}{\partial \psi}\right] \qquad (9)$$

3.2. Dimensionless Groups

Equations (8) and (9) can be expressed in a dimensionless form through the following dimensionless parameters:

$$u = \frac{\bar{u}}{U_1} \; ; \; k^* = \frac{\bar{k}}{k_1} \; ; \; c_p{}^* = \frac{\bar{c}_p}{c_{p1}} \; ; \; \mu^* = \frac{\bar{\mu}}{\mu_1}$$

$$X = \frac{x\,U_1}{\nu_1} \; ; \; E = \frac{\varepsilon}{\nu_1} \; ; \; P_{r1} = \frac{\mu_1\,c_{p1}}{k_1} \; ; \; \rho^* = \frac{\bar{\rho}}{\rho_1}$$

$$Y = \frac{U_1\,r}{\nu_1} \; ; \; p = \frac{\bar{p}}{0.5\,\rho_1\,U_1^2} \; ; \; P_{rt} = \frac{\varepsilon}{\varepsilon_H}$$

$$\theta = \frac{\left(\bar{T}-T_1\right)}{\left(T_{wr}-T_1\right)} \; ; \; L_m = \frac{U_1\,l_m}{\nu_1}$$

$$M_1 = \frac{U_1}{\left(\gamma R\,T_1\right)^{1/2}} \; ; \; \psi^* = \frac{\psi}{\nu_1}\left(\frac{U_1}{\rho_1}\right)^{1/2}$$

After substitution of these parameters and regrouping, equations (8) and (9), in X - ψ^* coordinates, become:

$$u\frac{\partial u}{\partial X} = -\frac{1}{2\rho^*}\frac{dp}{dX} + \frac{u}{2\psi^*}\frac{\partial}{\partial \psi^*}\left(S\frac{\partial u}{\partial \psi^*}\right) \qquad (10)$$

$$u\,c_p{}^*\frac{\partial \theta}{\partial X} = \frac{C_L}{2\rho^*}u\frac{dp}{dX} + \frac{C_L u S}{2\psi^*}\left(\frac{\partial u}{\partial \psi^*}\right)^2 + \frac{u}{2\psi^*}\frac{\partial}{\partial \psi^*}\left(Q\frac{\partial \theta}{\partial \psi^*}\right) \qquad (11)$$

Where:

$$C_L = \frac{(\gamma - 1)M_1^{\,2}}{\frac{T_{wr}}{T_1} - 1}$$

$$Q = \left(\frac{\mu^*}{P_{rl}} + \frac{E\rho^*}{P_{rt}}\right)\frac{Y^2\rho^* u}{2\psi^*}$$

$$S = \left(\frac{\mu^* + E\rho^*}{2\psi^*}\right)Y^2\rho^* u$$

3.3. Turbulent Shear Stress and Heat Transfer

The well-known Prandtl assumption for the turbulent shear stress and heat transfer is:

$$\varepsilon = l_m{}^2\frac{\partial \bar{u}}{\partial r} \qquad (12)$$

In a dimensionless form and X - ψ^* coordinates, equation (12) becomes:

$$E = \frac{u\rho^* Y}{2\psi^*}L_m{}^2\left|\frac{\partial u}{\partial \psi^*}\right|$$

For specifying the approximate relationship between the mixing length and the mean flow variables, confined jet mixing, as reported in [14], can be split into several distinctive regions as shown in Fig. (3). The first region is called regime-1, which contains the wall boundary layer, jet shear layer, secondary and primary potential flow regions. While the second one is called regime-2 which contains a single region of developing flow. The methods of estimating mixing length are different in each flow region.

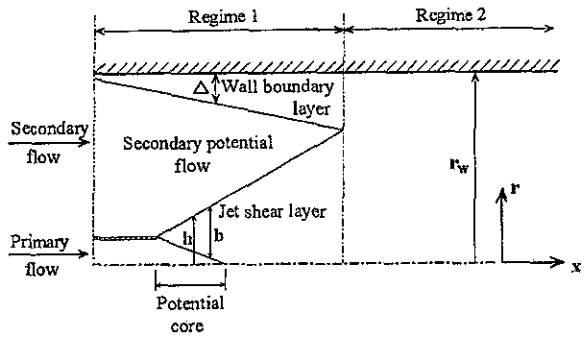

Fig. (3) Flow regions.

3.3.1 The jet shear layer

The mixing length is assumed to be dependent only on the shear layer width,

$$L_m = \text{function (b)}$$

$$(h - b) < r < h \quad , \quad L_m = k_o\, b \qquad (13)$$

The effect of compressibility on the mixing length coefficient k_o, to which was assigned a value of 0.08, has been reported by Hedges and Hill [14], to be equivalent to multiplying k_o by D_C, which is defined by:

$$D_C = \left(0.66 + 0.34\exp\left(-3.42\,M_m{}^2\right)\right)^{1/2} \qquad (14)$$

Where M_m is the Mach number evaluated at the radial position where the local velocity is the arithmetic mean of the secondary and centerline velocities.

3.3.2 The wall boundary layer

Dimensional analysis of the variables known to affect the wall boundary layer mixing length yields:

$$\frac{L_m}{\Delta} = \text{function}\left(y^+, \frac{Y_w - Y}{\Delta}\right)$$

Where;

$$y^+ = \frac{r_w - r}{\bar{\mu}}(\tau\bar{\rho})^{1/2}$$

The following forms were used in regime-1 in the wall boundary layer:

$$0 < (Y_w - Y) \le A \quad , \quad L_m = 0.41(Y_w - Y) \qquad (15)$$

$$A < (Y_w - Y) \le \Delta \quad , \quad L_m = k_o\,\Delta \qquad (16)$$

The "change-point" A, is defined as the point at which the viscosity model predicts a larger value of L_m than $k_o\,\Delta$ and k_o is a mixing length coefficient, to which was assigned a value of 0.09. The definitions of the wall boundary layer thickness and shear layer thickness were based on the value of r at which the local velocity was 0.99 of the external stream velocity. In regime-2; the downstream mixing length distribution adopted is:

$$(Y_w - Y) < \frac{k_2 D_c}{0.41} \quad , \quad L_m = 0.41 (Y_W - Y) \qquad (17)$$

$$(Y_w - Y) \geq \frac{k_2 D_c}{0.41} \quad , \quad L_m = k_2 Y_w D_c \qquad (18)$$

In which k_2 is the downstream mixing length coefficient, to which was assigned a value of 0.28.

To prevent an abrupt change in the mixing length distribution at the end of Region-1, a transition distance was introduced, over which the mixing length distribution varied linearly with X between the upstream distribution at the end of Region-1 and the value obtained by equation (18), i.e., for

$$X_1 < X < (X_1 + X_L)$$

$$\frac{L_m}{Y_w} = f_1\left(\frac{Y}{Y_w}\right) + \left(\frac{X - X_1}{X_L}\right)\left[f_2\left(\frac{Y}{Y_w}\right) - f_1\left(\frac{Y}{Y_w}\right)\right]$$

Where;

$f_1\left(\frac{Y}{Y_w}\right)$ is the distribution at the end of regime-1

$f_2\left(\frac{Y}{Y_w}\right)$ is the distribution given by equation (18)

X_1 is the value of X at the end of regime-1

X_L is the transition length, arbitrary sit at 6 mixing section diameters.

The fluid properties were evaluated as follows:

The turbulent Prandtl number was assumed equal to 0.9. The ideal gas law provides;

$$\rho^* = \frac{\bar{\rho}}{\rho_1} = \frac{\bar{p}\, T_1}{p_1\, \bar{T}}$$

For viscosity, Sutherland's formula [15] can be used ;

$$\mu^* = \frac{\bar{\mu}}{\mu_1} = \left(\frac{\bar{T}}{T_1}\right)^{3/2}\left[\frac{T_1 + C_2}{\bar{T} + C_2}\right]$$

Where C_2 = 110 K for air. The molecular Prandtl number and specific heat were assumed constant, so that

$$C_p^* = 1$$

$$k^* = \frac{\mu^* C_p^*}{P_r^*} = \mu^*$$

3.4 Finite Difference Equations

The general form of differential equations (10 and 11) summarized in table (1) in finite-differencing form according to grid lines shown in Fig.(4) is:

$$A_{n-1}\, \beta_{m+1,n} + B_{n-1}\, \beta_{m+1,n+1} + C_{n-1}\, \beta_{m+1,n-1} = D_{n-1} \qquad (19)$$

Table (1) differential equations in finite-difference form

Variables	β	A_{n-1}	B_{n-1}	C_{n-1}	D_{n-1}
Momentum	u	$Z_1 + Z_2 + \frac{u_{m,n}}{\Delta X}$	$-Z_1$	$-Z_2$	$-\frac{1}{4\rho^*_{m,n}}\left(\left.\frac{dp}{dX}\right\|_m + \left.\frac{dp}{dX}\right\|_{m+1}\right) + \frac{u_{m,n}^2}{\Delta X}$
Energy	θ	$Z_3 + Z_4 + \frac{u_{m,n}}{\Delta X}$	$-Z_3$	$-Z_4$	$\frac{u_{m,n}\,\theta_{m,n}}{\Delta X} + \frac{C_L u_{m,n} S_{m,n}}{2\psi^*}\left(\frac{\Delta\psi_2\left(u_{m,n+1} - u_{m,n}\right)}{\Delta\psi_1\left(\Delta\psi_1 + \Delta\psi_2\right)} + \frac{\Delta\psi_1\left(u_{m,n} - u_{m,n-1}\right)}{\Delta\psi_2\left(\Delta\psi_1 + \Delta\psi_2\right)}\right)^2 + \frac{C_L u_{m,n}}{4\rho^*_{1,n}}\left(\left.\frac{dp}{dX}\right\|_m + \left.\frac{dp}{dX}\right\|_{m+1}\right)$

Where;

$$Z_1 = \frac{u_{m,n}}{2\psi^*_n}\left(\frac{S_{n+1} + S_n}{\Delta\psi_1\left(\Delta\psi_1 + \Delta\psi_2\right)}\right)$$

$$Z_2 = \frac{u_{m,n}}{2\psi^*_n}\left(\frac{S_n + S_{n-1}}{\Delta\psi_2\left(\Delta\psi_1 + \Delta\psi_2\right)}\right)$$

$$Z_3 = \frac{u_{m,n}}{2\psi^*_n}\left(\frac{Q_{n+1} + Q_n}{\Delta\psi_1\left(\Delta\psi_1 + \Delta\psi_2\right)}\right)$$

$$Z_4 = \frac{u_{m,n}}{2\psi^*_n}\left(\frac{Q_n + Q_{n-1}}{\Delta\psi_2\left(\Delta\psi_1 + \Delta\psi_2\right)}\right)$$

3.5 Boundary Conditions

Along the axis of symmetry, the following boundary conditions were used:

$$Y = 0 \quad ; \quad \psi^* = 0 \quad ; \quad \frac{\partial u}{\partial \psi^*} = 0 \quad ; \quad \frac{\partial \theta}{\partial \psi^*} = 0$$

And the wall boundary conditions are:

$Y = f(X)$ (known wall geometry) ;

$$\psi^* = \text{constant} \quad ; \; u = 0 \quad ; \quad \frac{\partial \theta}{\partial \psi^*} = 0$$

3.6 Solution Procedure

1- A precise specification will often not be essential because the mathematical nature of the parabolic equations is such that major portion of the flow will not be affected by small changes in these conditions. For this reason, the dimensionless eddy viscosity was initialized at zero, and "top-hat'' velocity and temperature profiles (uniform values in primary and secondary streams) were assumed.

2- The calculation procedure starts with the upstream flow boundary, where the values of all flow variables must be known or assumed. The known Initial conditions, m = 1 line, as shown in Fig. (4), are related to the unknown conditions, m = 2 line, by the previously derived equations, and known boundary conditions.

3- A set of N-2 simultaneous algebraic equations are obtained and the coefficients of these equations form a tridiagonal matrix except for the initial and final rows which only contain two terms.

4- Rapid and exact solution to a tridiagonal matrix is obtained using the Thomas algorithm. Thomas algorithm uses a successive elimination technique. The Solution for the variables is iterative, the procedure adopted was to estimate the pressure gradient and solve the equations using the algorithm.

5- The equations automatically satisfy conservation of mass, momentum and energy, but only one pressure gradient yields the correct wall geometry.

6- The duct radius corresponding to the estimated pressure gradient was calculated from the M = 2 line variables. The pressure gradient was then incremented by a small percentage of its initial estimated value, and the calculation process is repeated for a new duct radius.

7- A third estimate of the pressure gradient was obtained by interpolation between the calculated, and the actual duct radii. In all the calculations performed, this value has been acceptably close, within 0.001 percent, to the actual duct radius. If this condition is not met, a further iteration is applied until reaching the proper solution.

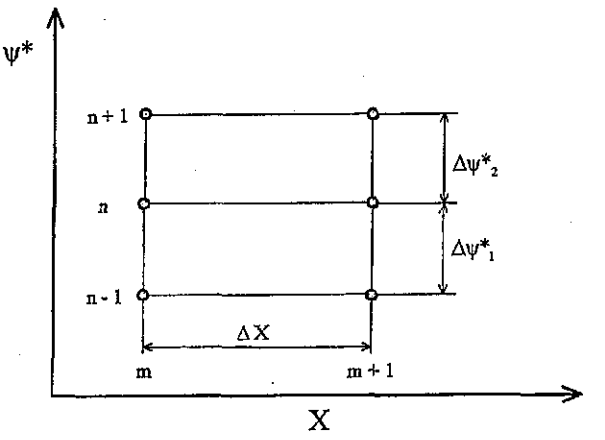

Fig. (4) Grid lines used in finite difference equations.

3.7 Model Verification

In order to extend the theoretical study, the model must be firstly validated. The model has been tested against published experimental and analytical results of [3]. These comparisons are presented in Figs. (5-7) under the same conditions of motive stagnation pressure and temperature, P_{o1} & T_{o1} through the tested ejector. It is evident from Fig. (5) that the present predicted wall static pressure distributions and experimental one [3] are in closer agreement than the predicted and experimental of [3]. While Figs. (6,7), show the present predicted, experimental and theoretical velocity and temperature profiles at four axial locations of [3].The comparison show acceptable agreement. The discrepancy of results may be due to the empirical input of the velocity and temperature profiles into the analytical model presented in [3].

The model has been also validated against the present experimental results as shown in Fig. (8), for wall static pressure coefficient distributions at five different values of motive stagnation pressure coefficient. The comparison is in a reasonable agreement.

4. RESULTS AND DISCUSSION

4.1 Effect of motive flow stagnation pressure, P_{o1}

Effect of motive flow stagnation pressure is studied for an isothermal flow, where the temperatures of both motive and entrained flows are 300 K. Effect of motive stagnation pressure coefficient on wall static pressure coefficient distributions along the tested ejector is shown in Fig. (9). While its effect on centreline Mach number is illustrated in Fig. (10), the highest motive stagnation pressure coefficient line, 4 shows an increase in Mach number due to extension of the supersonic regime in the convergent part of the mixing duct. Velocity profiles at seven axial locations are shown in Fig. (11). It can be seen at locations $x / R_o = 9.1$ and 12.29 that the velocity profiles are nearly the same, this is

because complete mixing and fully developed flow have already been accomplished and the length of the constant area section is longer than the required length.

The detailed Mach number contours are given in Fig. (12) at different values of C_{P_o}. It can be concluded that an earlier mixing is accomplished with a lower stagnation pressure coefficient. Figure (13) represents the effect of motive stagnation pressure coefficient on the ejector efficiency and pressure ratio for three different mass ratios. Here the ejector efficiency is defined as:

$$\eta = \frac{\text{Useful power}}{\text{Input power}} = \frac{V_2}{V_1}\frac{(P_{oe} - P_{o2})}{(P_{o1} - P_{oe})} = \mu \frac{T_2}{T_1}\frac{\phi}{(1-\phi)}$$

It is clear from Fig. (13) that the ejector efficiency decreases with decreasing the mass ratio. Also the results reveal that at constant mass ratio, the efficiency is improved by increasing the motive stagnation pressure coefficient until the pressure ratio becomes remarkably small. While Fig. (14) illustrates the effect of motive stagnation pressure coefficient on ejector efficiency and pressure ratio for four different values of temperature ratio. It is noticed that at a certain value of motive stagnation pressure coefficient, the ejector efficiency is enhanced by decreasing the temperature ratio. This may be due to a decrease in the input energy to the ejector system represented in a decrease in the primary flow static temperature, see the above efficiency definition. It is well known that a larger motive stagnation pressure results in a lower mass ratio , a larger entrained mass flow rate and consequently a lower efficiency.

4.2 Effect of temperature ratio, λ

The critical motive mass flow rate passing through the motive nozzle decreases by increasing its stagnation temperature (higher values of λ), which results in a lower jet velocity, lower Mach number, and a higher static pressure at the nozzle exit plane. The entrained flow stagnation temperature is kept constant, T_{o2} = 300 K, while that of the motive flow, T_{o1} is varied in order to investigate the effect of temperature ratio on the ejector performance.

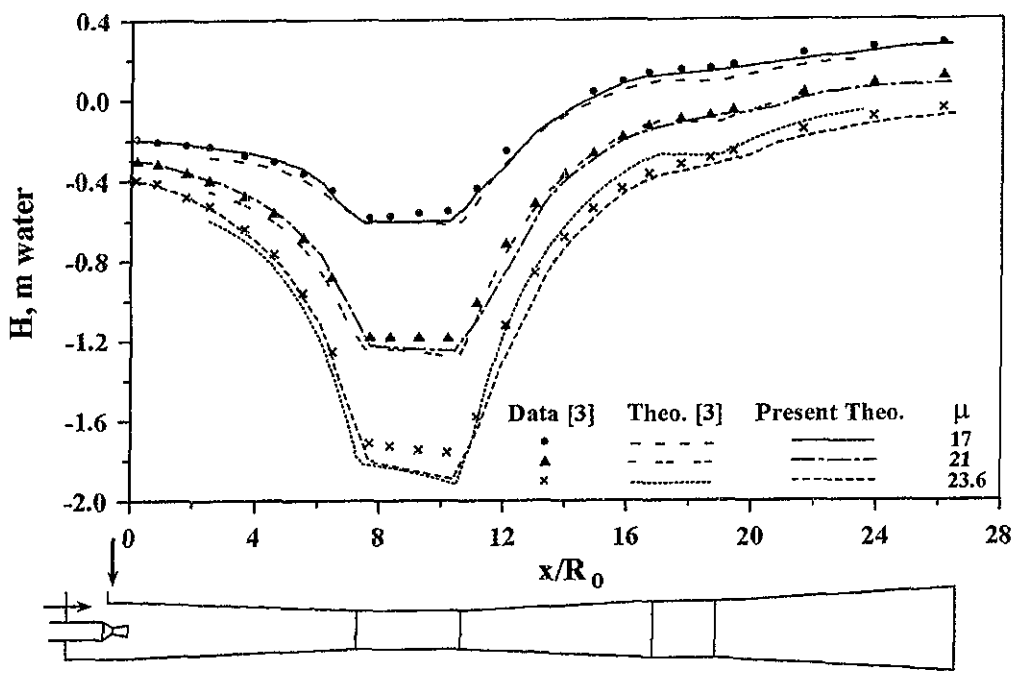

Fig. (5) Comparison between predicted wall static pressure distributions and published theoretical and experimental data, Ref. [3] for different entrainment ratios. (P_{O1} = 24 bar , T_{O1} = 706 K)

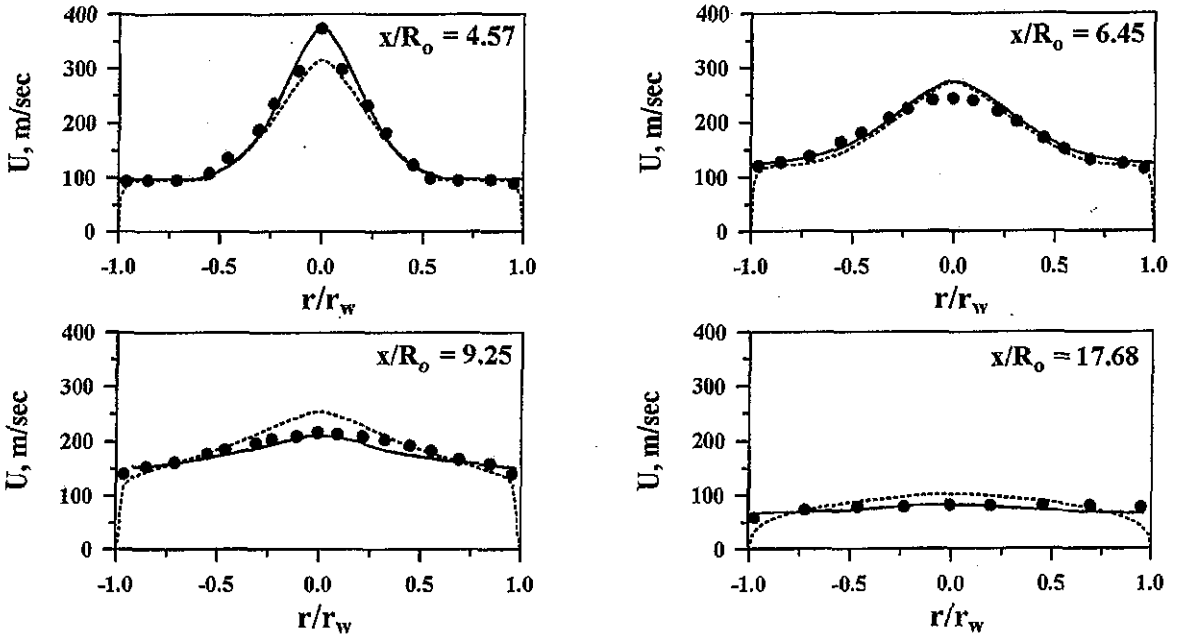

Fig. (6) Comparison between predicted radial variation of axial flow velocity, published theoretical and experimental data, Ref. [3], at four axial locations.
(P_{O1} = 24 bar, T_{O1} = 706 K)

Data, Ref.[3] ● **Theoretical, Ref.[3]** —— **Present theoretical** ---------

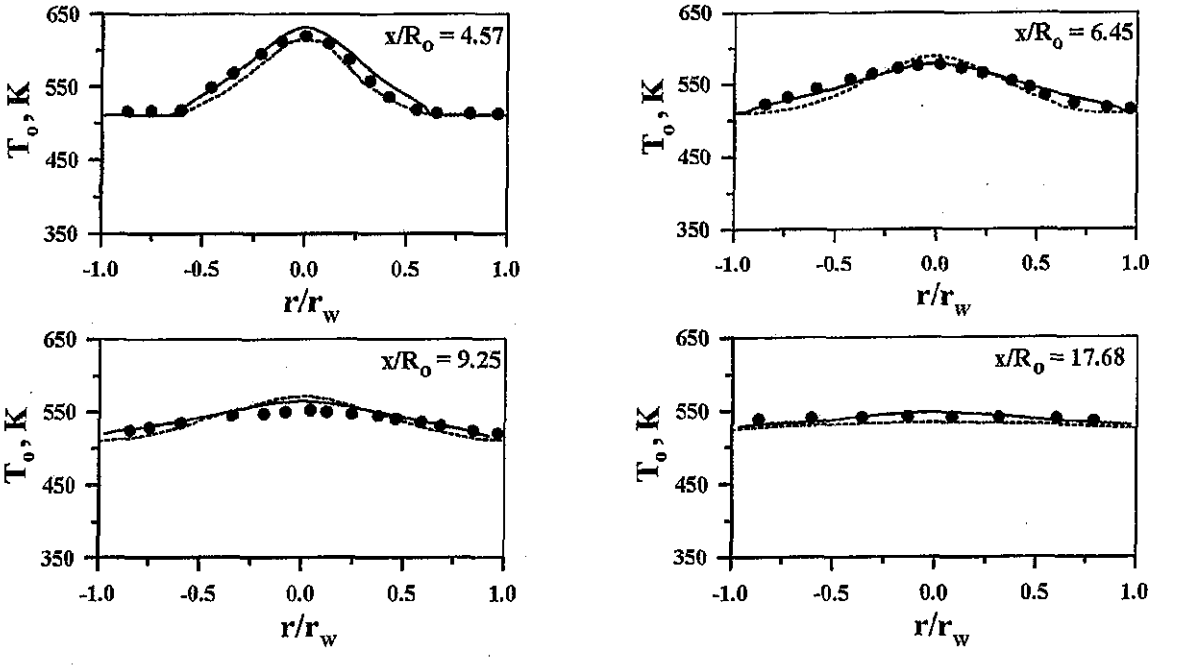

Fig. (7) Comparison between predicted radial variation of stagnation temperature, published theoretical and experimental data, Ref. [3] at four axial locations.
(P_{O1} = 24 bar, T_{O1} = 706 K)

Data, Ref.[3] ● **Theoretical, Ref.[3]** —— **Present theoretical** ---------

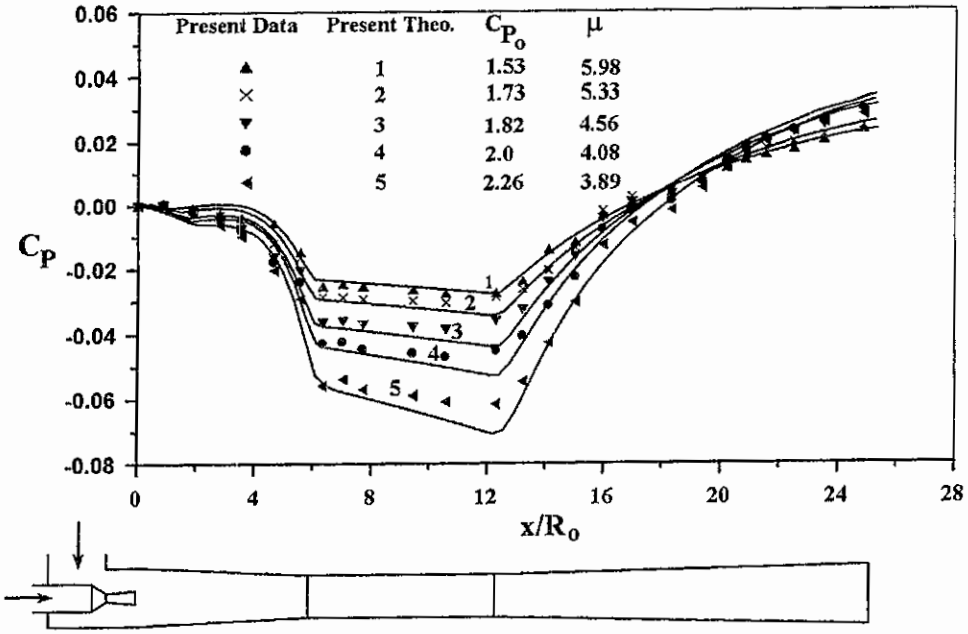

Fig. (8) Comparison between predicted wall static pressure coefficientdistributions and experimental data at different inflow conditions.

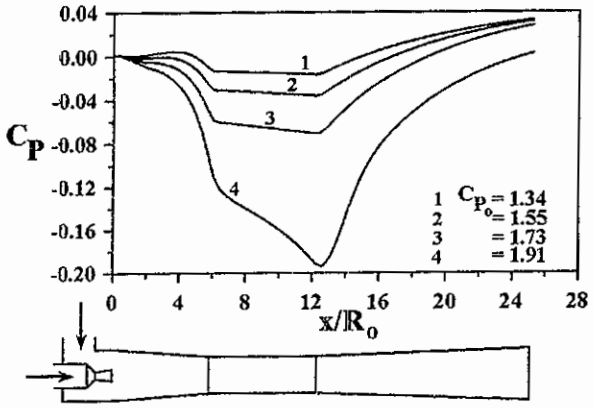

Fig. (9) Effect of motive stagnation pressure on pressure coefficient distributions, μ = 5.

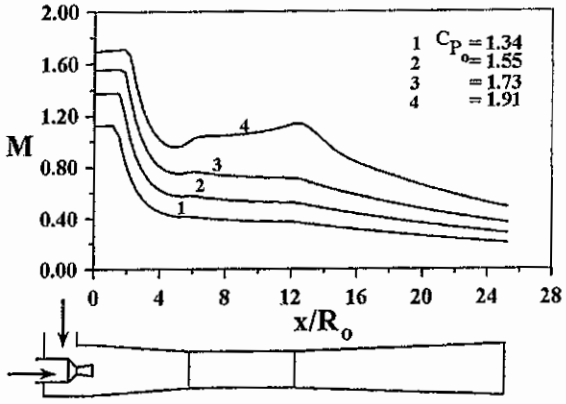

Fig. (10) Effect of motive stagnation pressure on centreline Mach number distributions, μ = 5.

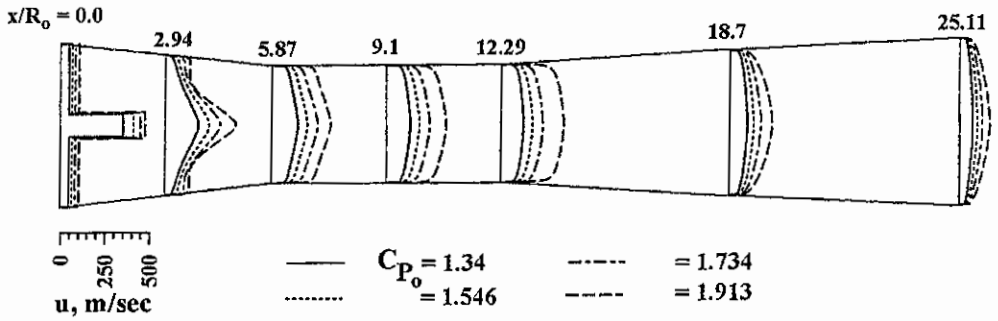

Fig. (11) Effect of motive stagnation pressure on velocity profiles along ejector at different locations, μ = 5.

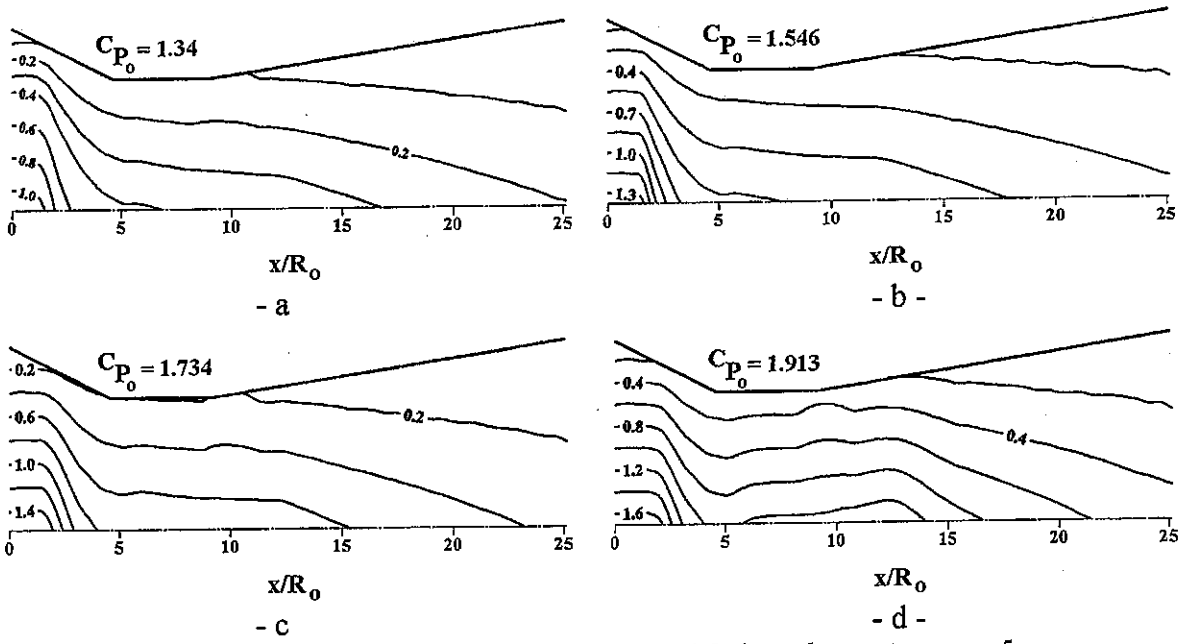

Fig. (12) Effect of motive stagnation pressure on Mach number contours, $\mu = 5$.

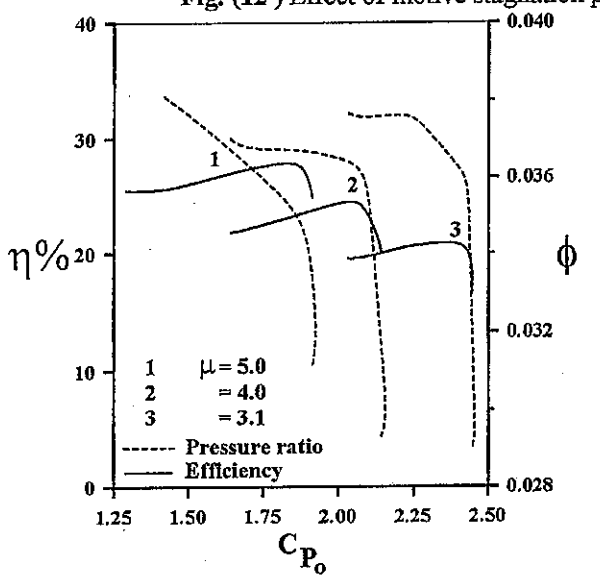

Fig. (13) Effect of motive stagnation pressure on ejector efficiency and pressure ratio, $\lambda = 1$.

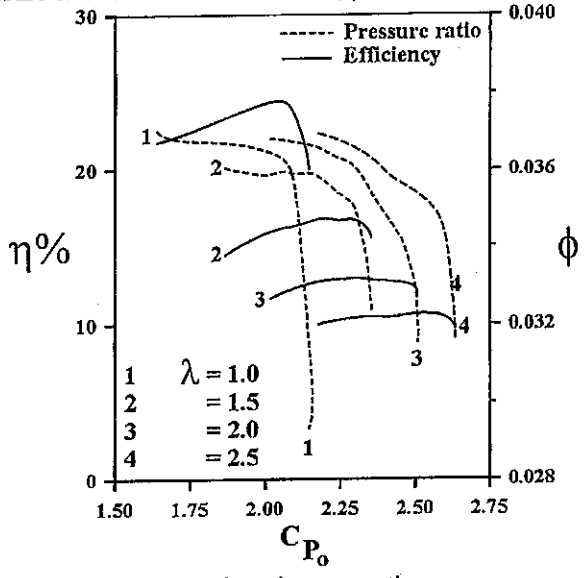

Fig. (14) Effect of motive stagnation pressure on ejector efficiency and pressure ratio, $\mu = 5$.

Figure (15) illustrates the effect of temperature ratio on the ejector efficiency and pressure ratio for four different mass ratios at a constant motive stagnation pressure coefficient. It is clear from the figure that at a certain value of λ, the efficiency is improved by increasing the mass ratio, while at constant mass ratio, increasing temperature ratio firstly increases the efficiency due to an increase in the total exit stagnation pressure, However efficiency is then decreased due to increasing the primary flow static temperature at the nozzle exit which is inversely proportional to ejector efficiency. Figure (16) shows the effect of temperature ratio on the ejector efficiency and pressure ratio for different motive stagnation pressure coefficients at constant mass ratio. From the figure it is seen that at a certain value of temperature ratio, the ejector efficiency is improved by increasing the motive stagnation pressure coefficient as a result to the increase in the total stagnation pressure at the ejector exit plane. A hotter entrained flow (smaller values of λ),increases the efficiency, while a larger motive stagnation pressure coefficient line has a lower efficiency due to an increased energy input represented in motive flow stagnation pressure.

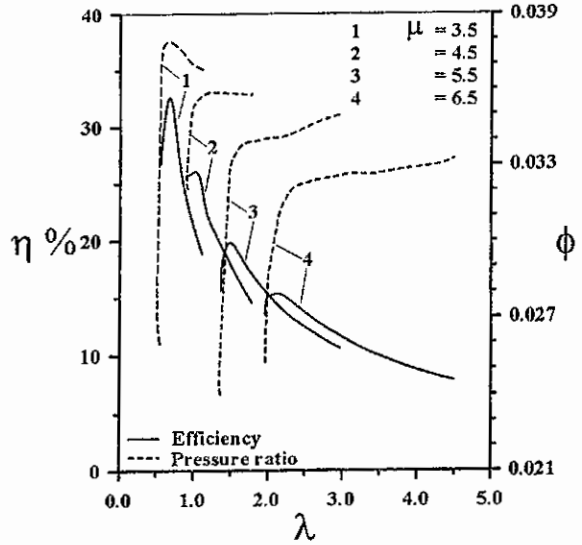

Fig. (15) Effect of temperature ratio on ejector efficiency and pressure ratio, C_{P_o} = 1.97.

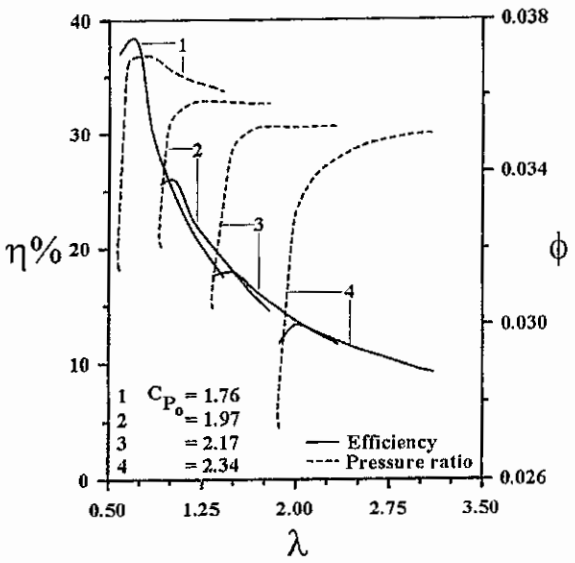

Fig. (16) Effect of temperature ratio on ejector efficiency and pressure ratio, μ = 4.5.

4.3 Characteristic curves of the tested ejector

The results obtained from the present study can be represented as shown in Fig. (17). The figure shows the dependence of operating parameters ϕ, C_{P_o}, η, λ and μ to each other for the tested ejector for the shown ranges of the parameters. From these curves, one may determine the suitable operating conditions to meet the required mass ratio μ. For example, if the required value of μ = 6 for an isothermal ejector under study (λ = 1), then the suitable motive stagnation pressure coefficient C_{P_o} should be about 1.54 which produces a pressure ratio ϕ of about 0.037 and the ejector has an efficiency of η = 31%.

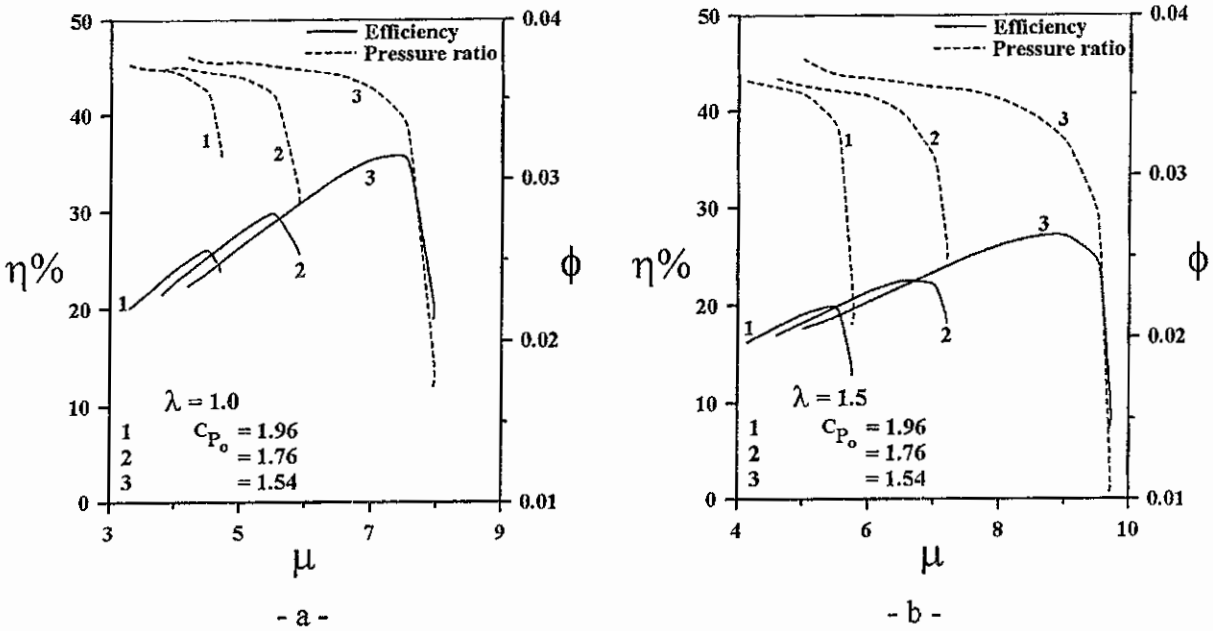

Fig. (17) Operational characteristic curves of the tested ejector at four different temperature ratios.

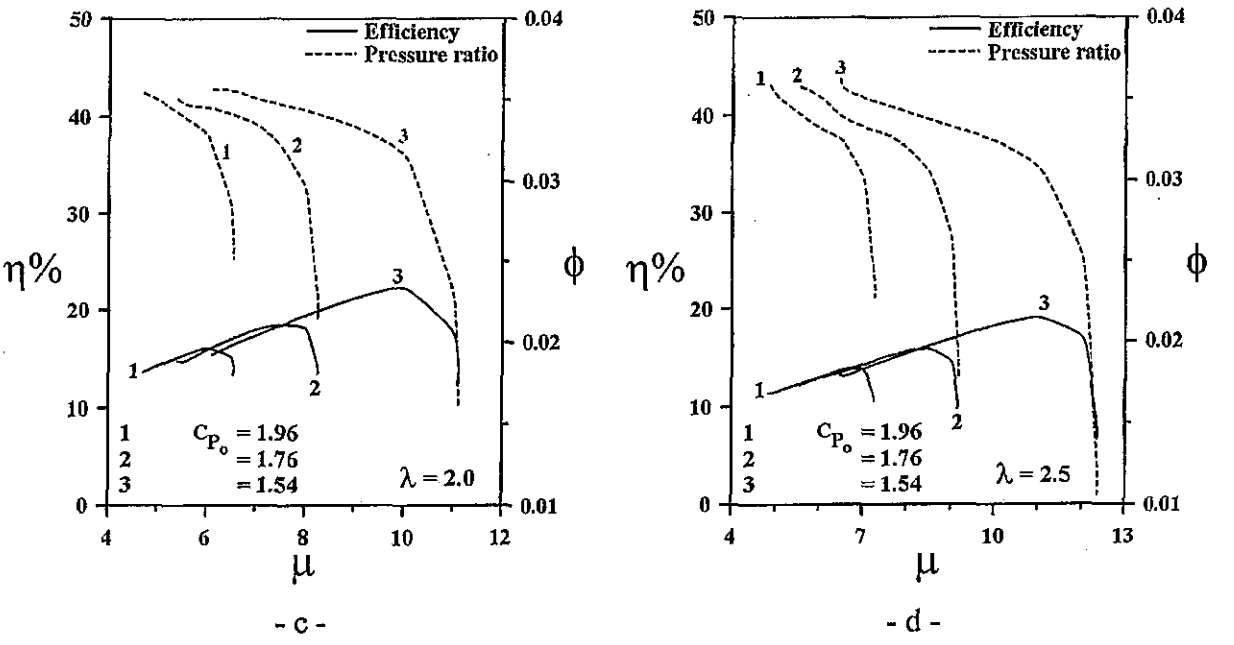

- c - - d -

Fig. (17) continued: Operational characteristic curves of the tested ejector at four different temperature ratios.

5. CONCLUSIONS

The present study deals with numerical and experimental investigation of supersonic air-air ejectors. The present theoretical and experimental results are compared with published data. The comparison shows a good agreement. Therefore, the obtained results help to understand the flow behaviour and physical phenomena occurring in the flow through ejectors. The operating conditions must be chosen carefully together with the dimensions of the ejector which greatly influence the ejector performance.

NOMENCLATURE

A_{n-1} *coefficient in equation (19)*

Ar area ratio, $(D_b/d)^2$

b local jet shear layer width

B_{n-1} coefficient in equation (19)

$\bar{c}_p$ time-average specific heat at constant pressure

c_p^* dimensionless specific heat, $\frac{\bar{c}_p}{c_{p1}}$

C_L Eckert number, $\frac{(\gamma - 1) M_1^2}{\frac{T_{wr}}{T_1} - 1}$

C_{n-1} coefficient in equation (19)

C_p wall static pressure coefficient, $\frac{P_i - P_1}{0.5\ \rho_1 u_1^2}$

C_{p_o} primary flow stagnation pressure coefficient, $\frac{P_{o1} - P_{ref}}{0.5\ \rho_1 U_1^2}$

d internal exit diameter of the primary flow nozzle

D diameter of the constant pressure mixing section at the nozzle exit plane

D_b diameter of the constant area mixing section

D_c mixing length compressibility correction factor

D_{n-1} *coefficient in equation (19)*

E dimensionless eddy viscosity, $\frac{\varepsilon}{\nu_1}$

H wall static pressure head

h distance from shear layer outer edge to the jet centreline

$\bar{k}$ time-average thermal conductivity

k* dimensionless thermal conductivity, $\frac{\bar{k}}{k_1}$

k thermal conductivity

l_m mixing length

L_m dimensionless mixing length

m^o mass flow rate

M mach number

M_1 primary flow mach number at nozzle exit plane, $\frac{U_1}{(\gamma R T_1)^{1/2}}$

$\bar{p}$ time-average static pressure

p dimensionless pressure, $\frac{\bar{p}}{0.5 \rho_1 U_1^2}$

P wall static pressure

P_o stagnation pressure

P_{ref} *reference atmospheric pressure*

P_{rt} turbulent Prandtl number, $\frac{\varepsilon}{\varepsilon_H}$

P_{r1} Prandtl number, $\frac{\mu_1 c_{p1}}{k_1}$

Q dimensionless parameter in equation (11)

q_T turbulent heat transfer, $\overline{(\rho v)' T'}$

R gas constant

R_o radius of the constant pressure mixing section at the nozzle exit plane

S dimensionless parameter in equation (10 and 11)

T local static temperature

$\bar{T}$ time-average temperature

T' instantaneous fluctuating temperature

T_o stagnation temperature

T_{wr} wall reference temperature

$\bar{u}$ time-average velocity in x-direction

u' instantaneous fluctuating axial velocity component

U local axial velocity in x-direction

u dimensionless velocity in x-direction, $\frac{\bar{u}}{U_1}$

$\bar{v}$ time-average flow velocity in r-direction

v' instantaneous fluctuating radial velocity component

x *space coordinate in the axial direction*

X dimensionless space coordinate, $\frac{U_1 x}{\nu_1}$

X_L transition length

ΔX step size in x-direction

y or r space coordinate in the radial direction.

Y dimensionless space coordinate in the radial direction, $\frac{U_1 r}{\nu_1}$

y^+ a variable used in the calculation of mixing length

V volume flow rate

α constant, unity for axisymmetric flow and zero for two-dimensional flow

η ejector efficiency

ϕ pressure ratio, $\frac{P_{oe} - P_{o2}}{P_{o1} - P_{o2}}$

γ ratio of specific heats

λ stagnation temperature ratio, $\frac{T_{o1}}{T_{o2}}$

ψ stream function

ψ^* dimensionless stream function, $\psi^{*2} = \frac{\psi^2 u_1}{\rho_1 v_1^2}$ (for axisymmetric flow)

ρ fluid density

$\bar{\rho}$ time-average fluid density

ρ^* dimensionless fluid density, $\frac{\bar{\rho}}{\rho_1}$

μ mass ratio, $\frac{m^\circ_2}{m^\circ_1}$

$\bar{\mu}$ time-average absolute viscosity

μ^* dimensionless absolute viscosity, $\frac{\bar{\mu}}{\mu_1}$

μ_1 primary flow viscosity at nozzle exit plane

τ local shear stress

τ_T turbulent shear stress, $\overline{(\rho v)' u'}$

ε eddy momentum diffusivity

ε_H eddy thermal diffusivity

θ dimensionless temperature, $\frac{\bar{T} - T_1}{T_{wr} - T_1}$

θ_1 total angle of constant pressure mixing section

θ_2 total angle of diffuser section

ν kinematic viscosity

δ local wall boundary layer thickness

Δ dimensional boundary layer thickness, $\frac{u_1 \delta}{\nu_1}$

k_o mixing length coefficient used in equations (13, 16)

k_2 mixing length coefficient used in equations (17, 18)

Subscripts

1 primary stream condition at nozzle exit plane

2 secondary stream condition at nozzle exit

plane
e mixing section exit condition
i an integer number denoting the pressure tap number or location of pressure
w wall condition

REFERENCES

[1] Fabri J. and Paulon J., "Theory and experiments on supersonic air-to-air ejectors", NACA TM-1410, September, 1958.

[2] Barna P. S., "Performance and noise generation studies of supersonic air ejector", NASA CR-2056, June, 1972.

[3] Hickman K. E., Hill P. G. and Gilbert G. B., "Analysis and testing of high entrainment and single-nozzle jet pumps with variable-area mixing tubes ", NASA CR-2067, June, 1972.

[4] Abou-Taleb F. A., "Effect of geometric parameters on the performance of ejectors", M.Sc. thesis, Department of mechanical engineering, Menoufia university, Egypt, 1986.

[5] Raman G. and Taghavi R., "Aeroacoustic Characteristics of a rectangular multi-element supersonic jet mixer-ejector nozzle ", Int. j. sound and vibration, Vol. 207(2), pp. 227-247, 1997.

[6] Huang B. J., Chang J. M., Wang C. P., and Petrenko V. A., "A 1-D analysis of ejector performance", Int. j. refrigeration, Vol. 22, pp. 354-364, 1999.

[7] De Chant L. J. and Nadell S. B., "A user's guide for the differential reduced ejector/mixer analysis "DREA" program", NASA TM-209073, April, 1999.

[8] De Chant L. J., Lear W. E., Sreadham P. L., Hunt P. L. and Holladay J. B., "Analysis and modeling of a two-phase jet pump of a thermal management system for aerospace applications", Int. j. mechanical engineering, Vol. 42, pp. 185-198, 2000.

[9] Szabo S., "Influence of the material quality of primary gas jets on the final vacuum created by a supersonic gas ejector", J. computational and applied mechanics, Vol. 2., No. 1., pp. 131-144, 2001.

[10] Arbel A., Shklyar A., Hershgal D., Barak M. and Sokolov M., "ejector irreversibility characteristics", J. fluids engineering, Vol. 125, pp. 121-129, 2003.

[11] Bartosiewicz Y., Zine Aidoun, Desevaux P. and Yves Mercadier, "Numerical and experimental investigations on supersonic ejectors", Int. j. heat and fluid flow, Vol. 26, pp. 56-70, 2005.

[12] Kandakure M. T., Gaikar V. G., and Patwardhan A. W., "Hydrodynamic aspects of ejectors", Chemical engineering science, Vol. 60, pp. 6391-6402, 2005.

[13] Krause E., "Numerical treatment of boundary-layer and Navier-Stokes equations", VKI lecture series, "Numerical methods in fluid mechanics", February 7-11, 1972.

[14] Hedges K. R. and Hill P. G., "Compressible flow ejectors", J. fluid engineering, Trans. ASME, Vol. 96, pp. 272-281, 1974.

[15] Schlichting H., "Boundary layer theory", McGraw-Hill Book, Inc., New York, 1968.